Thermal conductivity of InN with point defects from first principles

Carlos A. Polanco and Lucas Lindsay

Phys. Rev. B **98**, 014306 — Published 23 July 2018

DOI: 10.1103/PhysRevB.98.014306

Thermal conductivity of InN with point defects from first principles

Carlos A. Polanco and Lucas Lindsay
Materials Science and Technology Division, Oak Ridge National Laboratory, Oak Ridge, Tennessee 37831, USA

Thermal conductivity of InN with point defects from first principles

Carlos A. Polanco and Lucas Lindsay
Materials Science and Technology Division, Oak Ridge National Laboratory, Oak Ridge, Tennessee 37831, USA

Abstract

We present *ab initio* calculations of thermal conductivity of InN with vacancies and substitutional defects using a full solution of the Peierls-Boltzmann transport equation. Our parameter-free calculations are in good agreement with experimental measurements demonstrating the predictive power of this approach. Phonon-defect scattering rates are computed from a Green's function methodology that is non-perturbative and includes interatomic force constant variance induced near the defects. Restricting calculations to first order perturbation approaches can overestimate optic phonon scattering rates by nearly three orders of magnitude. On the other hand, neglecting the force variance weakens the scattering rates by about an order of magnitude, mostly in the low frequency region below 2 THz. This work elucidates important properties of phonon-defect scattering in thermal transport and demonstrates the predictive power of the coupling of Peierls-Boltzmann transport, Green's function methods and density functional theory.

I. INTRODUCTION

Defects are ubiquitous in crystalline materials and can provide significant thermal resistivity to heat-carrying phonons, especially at low temperatures or when defect concentrations are large [1]. Thus, accurately describing phonon-defect scattering is critical for predictive calculations of thermal conductivity, particularly toward understanding transport behaviors in device-relevant materials. Prevailing models for this type of scattering are limited to small perturbations [2], and typically only include perturbations to the vibrational equations of motion due to defect masses [1–3]. Often, these models are simplified further by assuming a linear phonon dispersion in combination with fitting parameters to match experimental data [1,4–7]. In spite of these simplifying assumptions, the models have been employed [7] and adapted [8] to describe the scattering of phonons by a variety of point defects (e.g., vacancies [8] and substitutions [6]), well beyond perturbation regimes and for which structural and force variances are large.

Recent *ab initio* calculations of phonon-defect scattering using a Green's function methodology [9], which is non-perturbative and includes variations of harmonic interatomic force constants (IFCs), coupled with Peierls-Boltzmann transport [10–15] have challenged fundamental intuition derived from the simplified perturbative methods. The Green's function approach has predicted unusually strong phonon-defect scattering rates arising from IFC variance for vacancies in Diamond [11], BAs [12], graphene [15], GaN [16] and FeSi [17], as well as for substitutions in SiC [13]. Including IFC variance also generates unexpected frequency trends of phonon scattering by dislocations in Si [14] and by substitutions in graphene [15]. With the few calculations available to date, we are just starting to gain insights from *ab initio* calculations of phonon-defect scattering beyond first order perturbation theory, particularly as relates to thermal transport and other functionalities. More calculations are required to continue benchmarking the Green's function methodology and reviewing our fundamental intuition of phonon-defect scattering.

Unfortunately, thermal conductivity measurements of crystalline materials with controlled defect types and densities are scarce. A prominent technique to create defects is to irradiate a sample with ions as done with GaN [18], InN [19] and graphene [7]. Of these, InN is less studied, though is a scientifically and technologically interesting material with a large phonon bandgap [20] and a small electronic bandgap. This material is useful for optoelectronic and photovoltaic applications [20] for which performance can depend critically on its thermal properties. More importantly for this study, measured InN thermal conductivity data is available as a function of irradiation dose, which can be correlated with vacancy defect density [19].

In this work, we examine phonon-point-defect interactions and their influence on the thermal conductivity of InN. We use the full solution of the Peierls-Boltzmann transport (PBT) equation coupled with a Green's function description of phonon-defect scattering, all built from interatomic forces derived from density functional theory (DFT). Specifically, we study the

conductivity of InN with indium (Vac_{In}) and nitrogen (Vac_N) vacancies as well as boron (B_{In}), aluminum (Al_{In}) and gallium (Ga_{In}) substitutions on the indium sites and arsenic (As_N) substitutions on the nitrogen sites (Sec. II). Our parameter-free calculations of thermal conductivity are compared with experimental values [17] (see Figure 1). The agreement of theory and experiment demonstrates the predictive capabilities of the PBT + Green's function methodology to model thermal conductivity of crystals with defects.

From this advanced numerical description of phonon-point-defect interactions we develop fundamental insights into phonon transport behavior and test previous intuition. We explore the changes in phonon-defect scattering from non-perturbative to first order perturbation approaches as well as from neglecting IFC variance induced by the defects via changes in structure and bonding (Sec. III). As expected, first order approximations fail at higher frequencies and for large mass variances. However, the magnitude of the deviation from non-perturbative methods is surprising. Scattering rates of optical phonons from As_N defects using first order perturbation theory are larger than the rates from the Green's function methodology by more than 3 orders of magnitude. This large difference may be important in studies of the dynamics of coherent optical phonons in the presence of defects [21–23], which are important for optoelectronic devices as introducing defects is a common way to increase switching speeds [22]. This discrepancy may also play a role in understanding Raman spectra in samples with defects [24,25].

The effect of neglecting the IFCs variance is also studied (Sec. III). We focus on the increase of scattering in the low frequency spectrum, which is important to correctly capture thermal transport at low and intermediate temperatures. Our calculations suggest that (1) the IFC contribution is proportional to the square of the relative change in the IFCs and (2) including IFC variance enhances scattering by allowing interactions between vibrations on different types of atoms. These insights help elucidate the role played by IFC variance on phonon-defect scattering.

II. THERMAL CONDUCTIVITY

We calculate the thermal conductivity κ of wurtzite InN with dilute point defects on In and N sites by summing over contributions from all phonons as

$$\kappa_\alpha = \frac{1}{\Omega}\sum_\lambda \hbar\omega_\lambda \frac{\partial n_\lambda}{\partial T} v_{\lambda\alpha}^2 \tau_{\lambda\alpha}, \quad (1)$$

with α a Cartesian direction, λ labeling the phonon branch and momentum, ω_λ the phonon frequency, n_λ the Bose-Einstein distribution, $v_{\lambda\alpha}$ the group velocity in the α direction, $\tau_{\lambda\alpha}$ the lifetime along the temperature gradient (also in the α direction), Ω the volume of the sample, $\hbar$ the reduced Planck constant and T the temperature. The thermal conductivity tensor for the hexagonal wurtzite structure can be described by two components, κ_x (in-plane) and κ_z (c-axis). The lifetimes are determined from the deviations from equilibrium of the phonon distributions that result from solving iteratively the linearized Peierls-Boltzmann transport

equation [1,26–32] including intrinsic 3-phonon scattering [1,26], phonon-isotope scattering [2] and phonon-defect scattering [9]. In our calculations we assume that phonons scatter independently from different defects (as expected in the 'dilute' limit), thus phonon-defect scattering rates depend only on the number of defects, not on their specific distribution. Details of these calculations as applied to InN are given in Appendix A. Here we elaborate further on *ab initio* calculations of phonon-defect scattering.

Phonon-defect scattering is computed using a Green's function methodology based on the so-called T-matrix T_d [9]. This approach captures the scattering due to mass and interatomic force constant variations (from structure and bonding) introduced by defects. These variations can be large; thus application of common perturbative methods is unjustified.

Within this Green's function methodology, the scattering rates of phonons due to a dilute and random distribution of defects is given by [9,33]

$$\frac{1}{\tau_\lambda^d} = -n_d \frac{\Omega_\lambda}{\omega_\lambda} Im\{\langle\lambda|T_d|\lambda\rangle\} \quad (2)$$

with n_d the number of defects per unit volume and Ω_λ the volume of the simulation domain containing the defect where phonon eigenvectors are normalized. Note that Eq. 2 implicitly assumes defects are in the dilute limit, i.e., phonons are scattered independently from defects at different locations. Large, correlated defect concentrations require careful consideration of supercell samplings, and are not considered here. The T-matrix is defined by [9]

$$T_d = [I - V_d G_0]^{-1} V_d \quad (3)$$

with I the identity matrix, $V_d = H_d - H_0$ the perturbation to the dynamical matrix of the perfect system H_0 with respect to the dynamical matrix of the system with the defect H_d and, G_0 the retarded Green's function of the perfect system defined as $G_0 = [\omega^2 I - H_0 - \Sigma]^{-1}$ with Σ the self-energy term accounting for the interaction of the atoms not included in H_0 with those included in H_0. Further details regarding the calculation of Σ and G_0 are available in the literature [9,34,35]. For all our calculations, H_d includes only one defect and thus n_d in Eq. 2 is the density of defects in the model system. Harmonic and anharmonic IFCs are the only inputs to the phonon scattering rates (intrinsic and from defects) and κ calculations, which are obtained from density functional theory using Quantum Espresso (QE) [36], a plane wave based software package. For each defect, IFCs were computed after the host supercell was relaxed. Further details of the calculations are given in Appendix A. Note that while the phonon-defect scattering rates depend on frequency, they do not depend on temperature as the IFCs are only calculated at zero temperature. However, this scattering can play an indirect role in shaping the temperature dependence of thermal conductivity as the phonon populations (Bose-Einstein distributions in Eq. 1) are both frequency and temperature dependent.

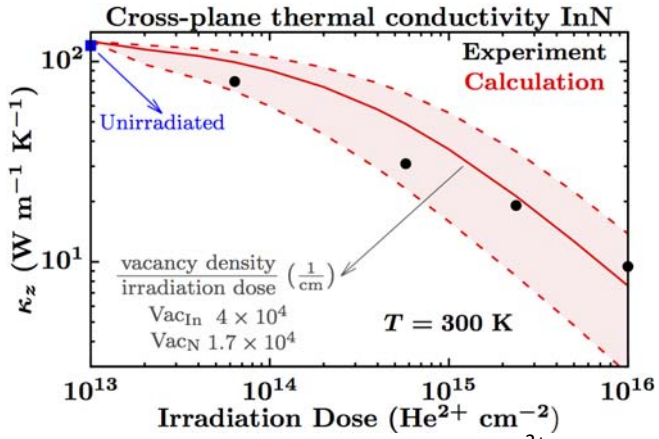

Figure 1: Cross-plane thermal conductivity as a function of He^{2+} ion irradiation dose. Measurements before (blue square, arbitrarily put on the y-axis) and after (black circles) irradiation are taken from Levander et al. [19]. Red curves are our *ab initio* calculations using the minimum (upper dashed), maximum (lower dashed) and average (solid) conversion factors to determine the number of In and N vacancies from irradiation dose. These are given in Table 1 [19].

Our *ab initio* calculations of cross-plane thermal conductivity for InN with indium and nitrogen vacancies are compared with measured values in Figure 1. The InN samples are single-crystal films with thickness varying from 0.5 to 2.1 µm, grown by molecular beam epitaxy [19]. The measured $Wm^{-1}K^{-1}$ for an unirradiated sample is close to the calculated $Wm^{-1}K^{-1}$ for InN with naturally-occurring isotope concentrations. The similarity of these values and their magnitude suggest that phonon-phonon interaction processes higher than third order [37] do not play a major role in determining the thermal conductivity of InN. Calculations also demonstrate that anisotropy and phonon-isotope scattering from natural isotopic variance are relatively small at 300K with and . The highly crystalline InN films were irradiated with a 2.13 MeV He^{2+} beam creating point defects (vacancies and interstitials) [19]. At room temperature, interstitials are thought to be generally mobile and may migrate and recombine at other defect sites, e.g. dislocations or at surfaces or interfaces [38]. On the other hand, vacancies are immobile [38]. Thus, we expect the density of interstitials to be much smaller than the density of vacancies [38] and we neglect phonon-interstitial scattering here. The distribution of vacancies after irradiation was determined to be relatively uniform across the samples [19]. Moreover, simulations provided a conversion factor to determine induced vacancy concentration from the irradiation dose (inset of Figure 1 of Levander et al. [19]). We use the minimum, average and maximum conversion factors to define the concentration of N and In vacancies as a function of irradiation dose (Table 1) in our calculations of . Interstitial defects are not considered in this work. Figure 1 shows our computations of cross-plane thermal conductivity on InN using the minimum, average and maximum concentrations of In and N vacancies. Phonon-vacancy scattering rates used in the calculation are shown in Figure 9(a) in Appendix A. The agreement between measured and calculated values of irradiated InN is reasonable, especially considering the lack of fitting

parameters. This successful benchmark demonstrates that predictive *ab initio* calculations of thermal conductivity are possible even in materials with significant point defect concentrations.

	In vac/dose (cm^{-1})	N vac/dose (cm^{-1})
minimum	2×10^4	0.4×10^4
average	4×10^4	1.7×10^4
maximum	14×10^4	7×10^4

Table 1: Ratio between vacancy concentration (cm^{-3}) and ion irradiation dose (cm^{-2}) used to define the minimum, maximum and average density of vacancies from a particular irradiation dose. These ratios are extracted from the inset in Figure 1 of Levander et al. [19].

Based on the agreement between theory and experiment in Figure 1, the dilute limit assumption seems to hold from irradiation doses of 10^{13} to 10^{16} $He^{2+}cm^{-2}$. Over this range, the concentration of In vacancies varies from 4×10^{17} to 4×10^{20} cm^{-3}. Equivalently, the number of vacancies changes from one vacancy every 160,000 atoms to one vacancy for every 160 atoms. Our model for phonon-defect scattering assumes that each impurity center scatters phonons independently. This dilute limit assumption holds as long as most of the heat is carried by phonons that lose their phase coherence - behave like particles - between scattering events (~ 1.5 nm for a dose of 10^{16} $He^{2+}cm^{-2}$). Phonon decoherence could arise due to the randomness of the defect distribution or due to phonon-phonon interactions [39–41]. Examination of the transition from the dilute limit to correlated defects or high defect concentrations requires simulations that consider the wave nature of phonons and phonon-phonon interactions. This is not considered here.

At 300K and for vacancy concentrations $<10^{17}$ (cm^{-3}), phonon-vacancy scattering in InN is not significant. However, as defect density n_d increases above $n_d = 10^{17}$ (cm^{-3}), phonon-vacancy scattering becomes stronger relative to the intrinsic phonon-phonon interactions. A 10% decrease of κ_z relative to that of unirradiated InN occurs for an irradiation dose of 2×10^{13} (cm^{-2}), corresponding to In and N vacancy concentrations of 8×10^{17} (cm^{-3}) and 3.4×10^{17} (cm^{-3}), respectively and simultaneously. Increasing the defect densities by an order of magnitude diminishes κ_z to 60% of that for the unirradiated sample. For larger vacancy concentrations, κ_z drops precipitously with defect density n_d as phonon-vacancy scattering becomes the dominant resistance. Note that with decreasing temperature similar behavior will occur as intrinsic phonon-phonon scattering varies $\sim 1/T$, while phonon-defect scattering is T-independent.

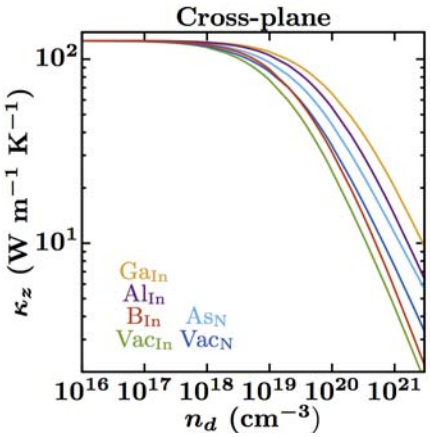

Figure 2: Cross-plane thermal conductivity of InN with B_{In}, Al_{In}, Ga_{In} or As_N substitutional defects as well as with In or N vacancies.

We also calculate the effects of substitutional defects on the thermal conductivity of InN. Specifically, we calculated thermal conductivity of InN with gallium (Ga_{In}), aluminum (Al_{In}) and boron (B_{In}) substitutions on In sites as well as with arsenic (As_N) substitutions on N sites. Calculations are given for cross-plane thermal conductivity values (Figure 2). Again, in-plane values are similar though slightly smaller (Figure 10). In general, substitutional atoms scatter phonons less effectively than vacancies, thus InN with substitutions tends to have higher than with vacancies. However, at higher defect densities, B_{In} defects scatter phonons more strongly than nitrogen vacancies due to larger phonon-defect scattering in the acoustic spectrum between 2 and 7 THz (Figure 9(b)). Note that acoustic phonons carry most of the heat, and in compound materials with a large mass difference between the constituent atoms, as in InN, the acoustic modes are governed by vibrations of the heavy atoms. Thus, defects on the In sites, particularly those that give large mass or force deviations, give a stronger suppression of the thermal conductivity than those on the light N atoms.

For In site substitutions, the relative scattering strengths follow common intuition as the mass difference increases (first row of Table 2) from Ga to Al to B, the resistance increases, in line with mass variance scattering in the Klemens and Tamura models [2,4]. The scattering strength due to B defects on In sites is also larger than that due to As defects on N sites. In this case, the larger mass variance of the As_N defect is compensated by the smaller density of states from N vibrations in the acoustic spectrum (see Sec. III), thus these defects have less relevance to thermal transport. We summarize in Table 2 the defect densities necessary to reduce the thermal conductivity of unirradiated InN by 10% and 50%. Our calculations indicate that defect densities on the order of - (cm^{-3}) are required to appreciably decrease the thermal conductivity. Defect densities on the order of - (cm^{-3}) reduce the conductivity by 50%.

	Ga_{In}	Al_{In}	B_{In}	As_N	Vac_{In}	Vac_N

Mass variance	0.15	0.58	0.82	18.91	1	1
IFC variance	0.37	0.49	1.16	0.66	1.25	1.05
from Eq. 7	2.5	3.5	25.0	400.0	30.0	800.0
from Eq. 8	2.0	2.8	20.0	4.5	24.0	9.0
(cm^{-3}) when	7.15	5.18	2.29	2.85	1.32	1.63
(cm^{-3}) when	111.8	70.56	26.84	44.87	18.02	27.36

Table 2: The first two rows give the mass and force constant variances for the point defects studied here. is the difference between the defect mass and the mass of the atom replaced by the defect . is the average relative change of IFCs between defect and non-defect systems described in more detail below Eq. 7. The third and fourth rows give the value of extracted by fitting the low frequency scattering rates from the Green's function methodology with Eq. 7 and Eq. 8, respectively. The last two rows show the defect density necessary to reduce the thermal conductivity of unirradiated InN to 90% and 50% of its original value.

III. PHONON-DEFECT SCATTERING

Commonly used approaches to calculate phonon-defect scattering are restricted to small perturbations of the dynamical matrix only due to mass differences [2,4]. In spite of these critical limitations, the approximations are widely used to describe a variety of point defects, and they have laid the groundwork for our current physical intuition of phonon-defect scattering. The T-matrix approach does not suffer from these limitations as it includes IFC variance and is non-perturbative, though is more challenging to calculate. In this section, we explore the breakdown of prevailing approximations in describing phonon-defect scattering and develop new insights into these.

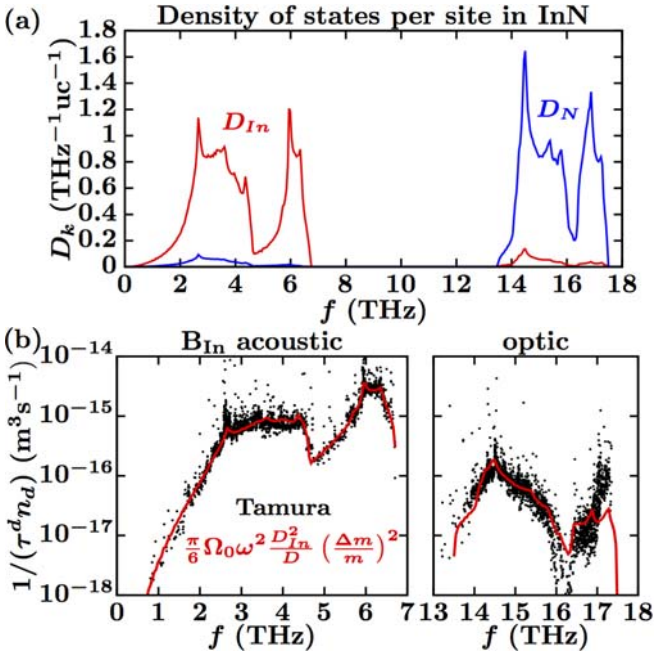

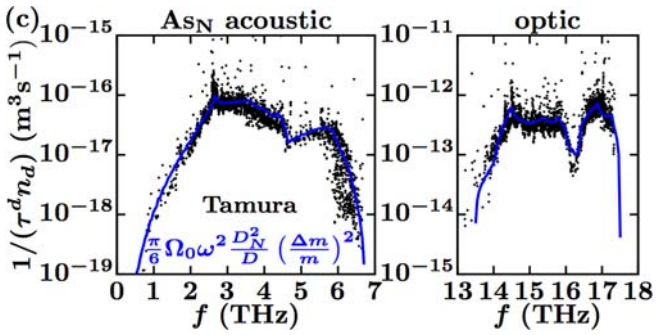

Figure 3: (a) Density of states of InN projected on an In site (red) and on a N site (blue). Note that the density of states is typically projected on an atomic type, which gives twice the density of states projected on a single site as shown in (a). Scattering rates normalized by defect density for B_{In} (b) and As_N (c) substitutions. Black dots are from the Tamura equation (Eq. 4), while solid curves are from Eq. 6 with from Table 2.

We use the Tamura expression [2], a first order perturbation description of phonon scattering from mass variance due to isotopes, as our baseline for examining phonon-defect scattering rates [2,42]

— —— (4)

with , and the fraction and mass of the type of atom in the th atomic site of the unit cell, the average mass of that site, and the eigenvector of the atom in the unit cell. This Tamura expression is similar to earlier approximations by Klemens [4] that gave rise to the empirical equations widely used today to describe phonon-defect scattering. For crystals with cubic symmetry, in Eq. 4 can be written as , and Eq. 4 simplifies to [3,43]

— – (5)

with — the projected density of states on atom . Note this is not the usual projected density of states on an atomic type, but it is projected on the single site . An example of for InN projected on an In and a N site is presented in Figure 3(a). For a relatively low concentration of mass defects on site , Eq. 5 can be further simplified by 1) noting that and , with , 2) replacing by its weighted average , with — the total density of states and, 3) summing over the sites that can host the defect so that with the defect density and the volume per unit cell. Following the steps outlined above we get

—— – ——— —— (6)

The scattering rates for B_{In} (solid red curves in Figure 3b) and As_N (solid blue curves in Figure 3c) using Eq. 6 closely track calculations using Eq. 4. The agreement demonstrates that the

scattering rates calculated from the Tamura equation are dictated by the square of the mass variance, the square of the phonon frequency and the square of the projected density of states divided by the total density of states.

To explore the differences between first order perturbation theory and the non-perturbative Green's function methodology, we compare the phonon-defect scattering rates calculated from the T-matrix approach including only mass variance (gray dots in Figure 4) with those from the Tamura expression (black dots in Figure 4). As expected, the two methods agree well in the low frequency region and for small mass variation, where the strength of the perturbations are weak [10]. For example, for Ga_{In} substitutions, the mass variance is small (0.15) and phonon-defect scattering rates from the two methods are similar over the entire frequency spectrum. For larger mass perturbations (first row of Table 2), particularly at higher frequencies, the two methods do not agree. For As_N substitutions the mass variance is two orders of magnitude larger (18.91) and the scattering rates of optical phonons from Tamura overestimate those from the T-matrix by more than three orders of magnitude. On the contrary, the scattering of optical phonons for Al_{In} and B_{In} substitutions is underestimated by Tamura by about an order of magnitude. Note that the disagreement between the T-matrix and Tamura rates indicates that the T-matrix rates do not follow the simple relations in Eq. 6.

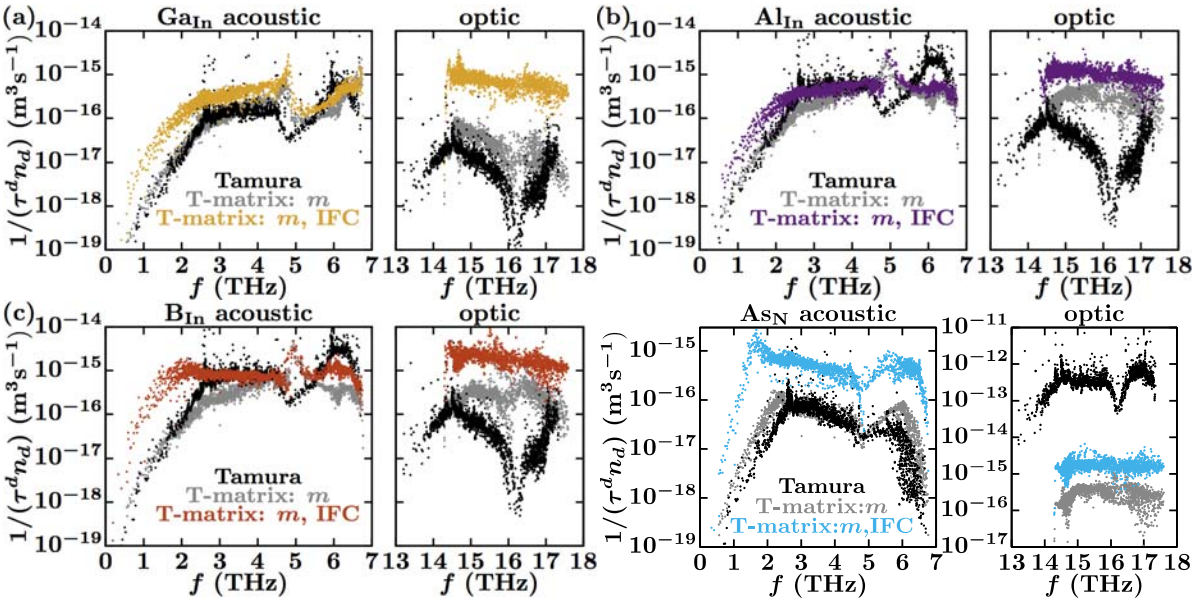

Figure 4: Phonon-substitution scattering rates in InN due to (a) Ga_{In}, (b) Al_{In}, (c) B_{In} and (d) As_N substitutions normalized by the defect densities. Black dots are the rates from the Tamura expression (Eq. 4), gray dots are the rates from the T-matrix approach (Eq. 2) including only mass variations. Colored dots are the rates from the T-matrix approach including mass and IFC variations.

To explore the effect of including the IFC variance, which is directly related to structural relaxation and bonding variations, we compare our T-matrix calculations varying only defect masses (gray dots in Figure 4) with varying both masses and IFCs (colored dots in Figure 4). In

general, including IFC variance increases the phonon-defect scattering rates over simple mass variance calculations. In the low frequency spectrum where the rates are proportional to ω^4, IFC variance gives a rigid upward shift of about an order of magnitude. This shift in the calculated rates may be important at lower temperatures where phonon-defect scattering is stronger than intrinsic scattering and low frequency phonons give larger contributions to transport.

To gain insights into the contributions from the IFC variance to the low frequency phonon-defect scattering rates below 2THz (colored dots in Figure 4), we fit these with a modification of Eq. 6

$$\frac{1}{\tau_{\lambda,k}^{d}} = n_d \frac{\pi}{6} \Omega_0 \omega_\lambda^2 \frac{D_k^2(\omega_\lambda)}{D(\omega_\lambda)} \left[\left(\frac{\Delta m_k}{m_k} \right)^2 + C_k \right] \quad (7)$$

C_k is a fitting parameter to capture the rates from the T-matrix calculation below 2 THz (colored dots in Figure 4) by shifting Tamura's rates upward. C_k gives a measure of the contribution to phonon-defect scattering from the IFC variance. An example of the fitting procedure for a Ga substitution on an In site is shown in Figure 5(a). When $C_k = 0$, Eq. 7 becomes Eq. 6 and the rates follow closely Tamura's expression (black dots in Figure 5(a)). The separation of mass and IFC contributions in Eq. 7 is inspired by an analytical derivation of the scattering rates for a 1D toy atomic chain. Figure 5(b) shows C_k as a function of the relative change in IFCs ($\Delta K_k / K_k$) for all the defects studied here. ΔK_k is the Euclidian norm of the difference between the IFC matrices of the system with and without the defect. K_k is the Euclidian norm of all the IFCs between the atom on site k and its neighbors in the system without the defect (see Table 2 for calculated values). Note that for vacancies, ΔK_k does not include the IFCs of the lost bonds. Figure 5(b) suggests that the fitting parameter C_k for defects on a particular site is a function of the square of the relative change in IFC ($\Delta K_k / K_k$), similar to $(\Delta m_k / m_k)^2$. This is evident from the data in Figure 5(b) following closely the dashed lines with slope 2.

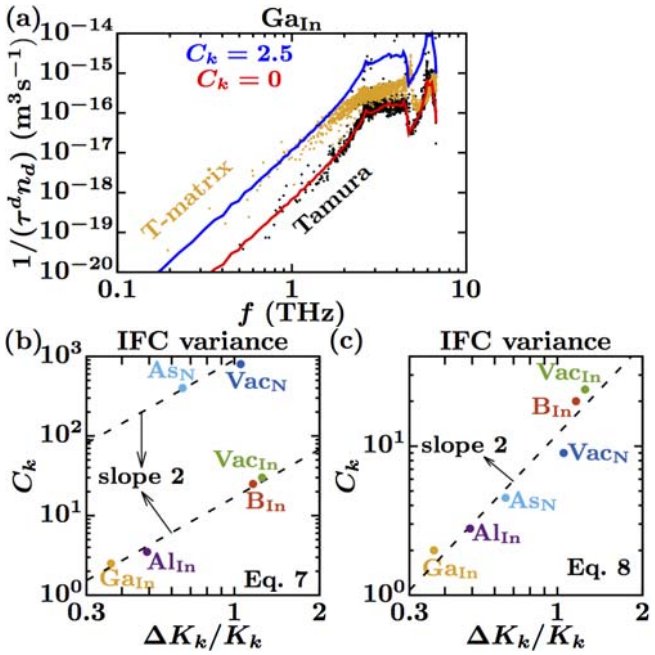

Figure 5: (a) Scattering rates from the Tamura (black dots) and T-matrix (yellow dots) methods for a Ga substitutional defect on an In site. The solid curves are given by Eq. 7 using from Table 2, (solid red curve) and (solid blue curve). Fitting parameter from Eq. 7 (b) and from Eq. 8 (c) that represents the contribution from the IFC variance to low frequency phonon-defect scattering rates below 2 THz (colored dots in Figure 4) for all the defects studied here. The dashed lines have slope 2.

Interestingly, the fitting procedure described above suggests that for defects on nitrogen sites is about 50 times larger than that on indium sites (see dashed lines in Figure 5(b)). Moreover, is about 8 times smaller than in the low frequency range, and this quantity is squared in Eq. 7. Based on these two observations and the expectation that similar should yield similar , we hypothesize that the scattering contribution from IFC variance should be proportional to the total density of states instead of the density of states projected on a particular site . Using this hypothesis, we fit the colored scattering rates in Figure 4 with the following equation

(8)

where divided by 4 represents the total density of states per atom in analogy with Eqs. 5 and 6. Figure 5(c) shows the results of the new fitting, where a single trend line with slope 2 seems to capture all the data. This suggests that the low frequency scattering rates are proportional to the square of the relative change in IFC for all of the point defects studied here, including vacancies and substitutions on nitrogen and indium sites.

The results of the fitting procedure of the scattering rates using instead of for the IFC variance contribution (Figure 5(c)) suggest that IFC variance breaks the restriction of phonon-defect scattering only arising from interactions between vibrations on the same atomic site. According to Eq. 4, which does not include IFC variance, the scattering of phonon to

phonon λ' is weighted by $\left|\boldsymbol{e}_k^{\lambda*} \cdot \boldsymbol{e}_k^{\lambda'}\right|^2$. This weighting factor restricts the scattering to interactions between vibrations on the same site, which is reflected in the scattering rates being proportional to $D_k(\omega_\lambda)$ (Eqs. 5, 6 and 7). We implicitly use this restriction when fitting C_k using Eq. 7 (Figure 5(b)). In this case for similar IFC variance, C_k for defects on nitrogen sites is larger than that on indium sites (Figure 5(b)). Relaxing the restriction improves the fitting (Figure 5(c)). Thus, including the IFC variance seems to allow phonon-defect scattering arising from interactions between vibrations on different atomic sites, which increases the scattering cross section and so the scattering rates. Although this hypothesis seems to work for InN, our preliminary calculations using Eq.8 for phonon-defect scattering in BAs does not give C_k on a single trend line with slope 2 for substitutions and vacancies, but rather on two separate lines with slope 2. This may suggest that other factors are also important in BAs, or that $\Delta K_k/K_k$ is not well defined.

Previously, we found unusual phonon-defect scattering rate behavior in graphene: decreasing rates with increasing frequency for flexural out-of-plane phonons interacting with nitrogen substitutions, which was explained in terms of IFC variance [15]. Figure 4(d) shows similar decreasing scattering rates with increasing frequency from about 1.5 to 4.5 THz for As_N defects. Here, however, this behavior seems to be driven by $\omega^2 D_k^2/D$ rather than the IFC variance. Note that the Tamura expression overestimates the mass variance scattering for the acoustic frequency range above 2.5 THz. This overestimation may compensate the neglected IFC variance.

IV. SUMMARY AND CONCLUSIONS

We examined lattice thermal conductivity of InN with vacancies and substitutional defects. Phonon-defect scattering rates are derived from a non-perturbative *ab initio* Green's function methodology including structural relaxation and variation of the interatomic forces local to the defect. These were incorporated into an *ab initio* full solution of the Peierls-Boltzmann transport equation to determine the thermal conductivity of InN with point defects. We demonstrate the predictive power of this parameter-free approach by comparing our calculations with measured thermal conductivity data for InN films with induced In and N vacancies. Defect densities between 1 to 7×10^{18} (cm^{-3}) are required to decrease the thermal conductivity of InN by 10%.

In general, we find that phonon scattering by substitutions is weaker than that by vacancies. Our results indicate that neglecting IFC variance weakens the phonon-defect scattering rates by about an order of magnitude in the low frequency spectrum. This difference is critical for calculations of intermediate temperature thermal conductivity, where phonon-defect scattering dominates and the low frequency phonons contribute more significantly to transport. We also find that first-order perturbation methods can overestimate the scattering rates of optical phonons by about three orders of magnitude. This large overestimation calls for a revision of methodologies that rely on first-order perturbation theory to capture the scattering of optical phonons with defects. Our calculations demonstrate that (1) at low frequencies the IFC variance contribution to the scattering rates is proportional to the square of

the relative change in the IFCs due to defects, and (2) including IFC variance increases the defect cross section beyond just mass variance, thus enhancing phonon-defect scattering rates.

V. ACKNOWLEDGEMENTS

C.A.P and L.L. acknowledge support from the US Department of Energy, Office of Science, Office of Basic Energy Sciences, Material Sciences and Engineering Division. This work used the Extreme Science and Engineering Discovery Environment (XSEDE) [44] (*TG-DMR160165*), which is supported by the National Science Foundation grant number ACI-1548562.

APPENDIX A: SIMULATION DETAILS

Harmonic Interatomic Force Constants (IFCs). We compute the harmonic IFCs from density functional theory (DFT) using the plane wave software package QUANTUM ESPRESSO [36]. Each IFC results from a numerical derivative of atomic forces by displacing individual atoms ± 0.04 Å from their equilibrium positions. The forces required for these finite displacement computations are determined from scf calculations using the pw.x module of QE on $4 \times 4 \times 3$ supercells of InN (192 atoms). Our scf calculations are done using cut-off energy of 60 Ry, electronic convergence threshold of 10^{-14} Ry, Gaussian smearing with degauss of 0.005 Ry, projected augmented-wave pseudopotentials [45] within the generalized gradient approximation PBESOL [46] (In.pbesol-dn-kjpaw_psl.0.2.2.UPF, N.pbesol-n-kjpaw_psl.0.1.UPF) and sampling only the Γ point of the Brillouin zone.

System without defects. We build the $4 \times 4 \times 3$ supercell for perfect wurtzite InN starting from a relaxed InN unit cell achieved from several vc-relax energy minimizations using the pw.x module with a $8 \times 8 \times 6$ sampling of the Brillouin zone with the grid displaced from the origin. This process gives lattice constants $a = 3.538$ Å and $c = 5.717$ Å, which are in agreement with experimental values $a = 3.534$ Å and $c = 5.709$ Å [47]. The IFCs calculated from atomic finite displacements in the supercell were considered to the 19th nearest neighbor shell. On that set, we enforce space group symmetry 186 and translational invariance using singular value decomposition and quadratic programing [48]. The calculated phonon dispersion is given by the solid lines in Figure 6, which agrees with experimental data [47] over the acoustic phonon spectra. Despite considering interactions to the 19th nearest neighbor shell, calculations deviate from the measured data for some of the high frequency optic modes as we did not include very long range Coulomb interactions that drive LO-TO splitting [49] in this region. Note also that the recursive algorithm used to calculate the Green's function in Eq. 3 relies on real space calculations and thus precludes incorporating reciprocal space methods for including long range forces.

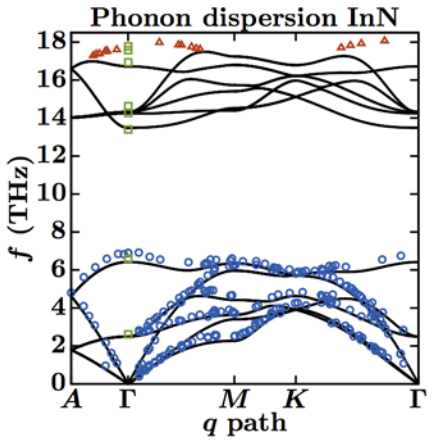

Figure 6: Calculated phonon dispersion of InN (solid curves) compared with measured data: blue dots [47], red triangles [50] and green squares [51].

System with defects. After inserting a point defect in a supercell, we relaxed the system until the interatomic forces are less than Ryd-Bohr^{-1} using vc-relax calculations with constant volume. In the relaxed state, the nearest neighbor distances for an atom in the defect supercell (not the defect itself) rapidly tend to those of the system without the defect (Figure 7). For each supercell with a defect, the IFCs were calculated using the finite displacement method described above and the space group symmetry was found to be 156 using the spglib library created by Togo [52] with a tolerance less than .

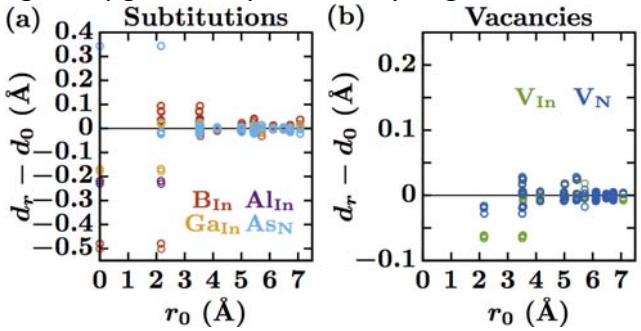

Figure 7: Changes in the distances of an atom to its nearest neighbors after a point defect is introduced and the supercell is relaxed. Given here is the difference between the nearest neighbor distances of an atom in an InN supercell with ( ) and without ( ) a defect versus the separation from that atom to the defect .

Green's function methodology. For the Green's function calculations, we use a rectangular supercell with 720 atoms as the simulation domain. The rectangular shape is convenient for calculations of the retarded Green's function of the perfect system , which are done by transforming to a set of decoupled 1D infinite chains following a procedure outlined by Mingo et al. [9]. We define the IFCs in the simulation domain by inserting the IFCs between atomic pairs within the 19th nearest-neighbor shells of the defect, found from finite displacements of the supercell with a defect, into the simulation domain. The inserted IFCs are modified slightly to enforce the point group symmetry of the defect as well as translational invariance on the whole simulation domain using singular value decomposition and quadratic programing [48]. Our scattering rates are well converged with

respect to the number of IFCs calculated within the simulation domain. Including IFCs between atomic pairs within the 19th and 17th nearest-neighbor shells of the defect yield similar scattering rates. As this set of IFCs decreases to those bounded by the 11th nearest-neighbor shells of the defect, the scattering rates of acoustic phonons decreases slightly (see Figure 8(a)). Decreasing the set of IFCs even more causes a decrease of the scattering rates of optical phonons as well as an increase in the scattering rates near 2 THz, likely due to changes in the IFCs when point group symmetries and translational invariance are enforced (see Figure 8(b) and 8(c)). The size of the simulation domain guarantees that atoms near the edges of the domain have IFCs equal to those of atoms in the perfect InN system. This ensures that the differences between dynamical matrices of the systems with and without the defect are zero outside the simulation domain.

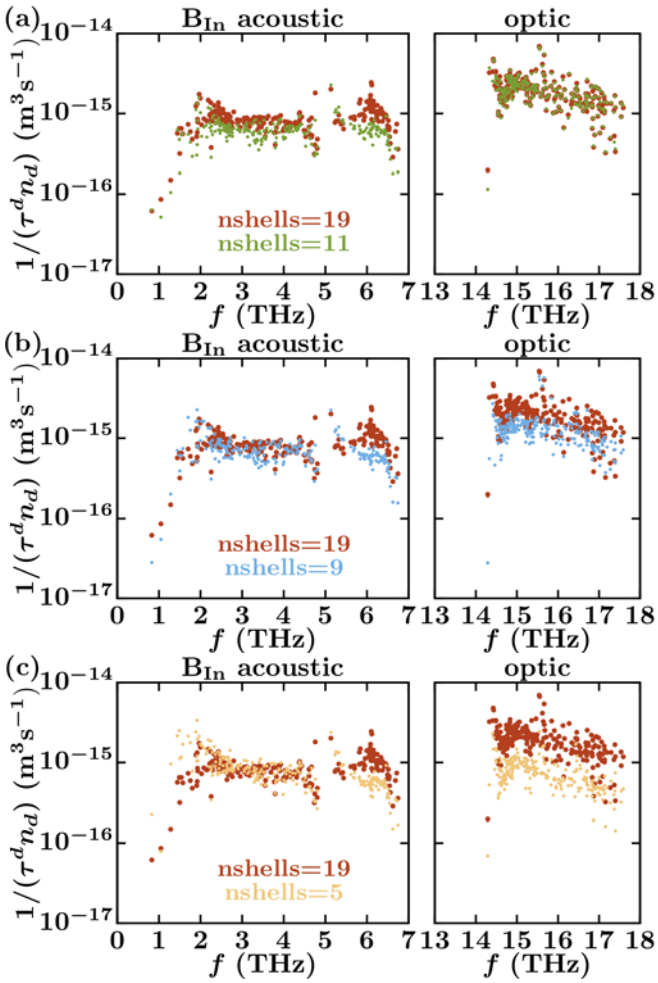

Figure 8: Phonon scattering rates due to a B substitution on an In site including IFCs between atomic pairs within the 11th (a), 9th (b) and 5th (c) nearest-neighbor shells of the defect.

Thermal conductivity. for InN with defects is calculated using the linearized Peierls-Boltzmann transport equation [1,26,31]

(9)

with and coefficients from three-phonon scattering processes defined in Ref. [28]. Phonon-defect scattering is included using the result from Eq. 2 and do not depend on the distribution of modes and as the three-phonon interactions do. Eq. 9 is solved iteratively [27] for the deviations from equilibrium for each phonon mode, which determine the transport lifetimes in Eq. 4, . The anharmonic IFCs required in this calculation are obtained in a similar manner to the harmonic IFCs above, though using 3x3x3 supercells and considering interactions to 5th nearest neighbors of the unit cell atoms. A subset of anharmonic IFCs were determined using 4x4x3 supercells and were similar within the numerical precision of the calculations.

APPENDIX B: SCATTERING RATES

Figure 9(a) gives the scattering rates due to vacancies used in the calculation of thermal conductivity of InN shown in Figure 1. Figure 9(b) demonstrates that the scattering rates due to B_{In} substitutions are larger than those due to nitrogen vacancies in the acoustic spectrum between 2 and 7 THz.

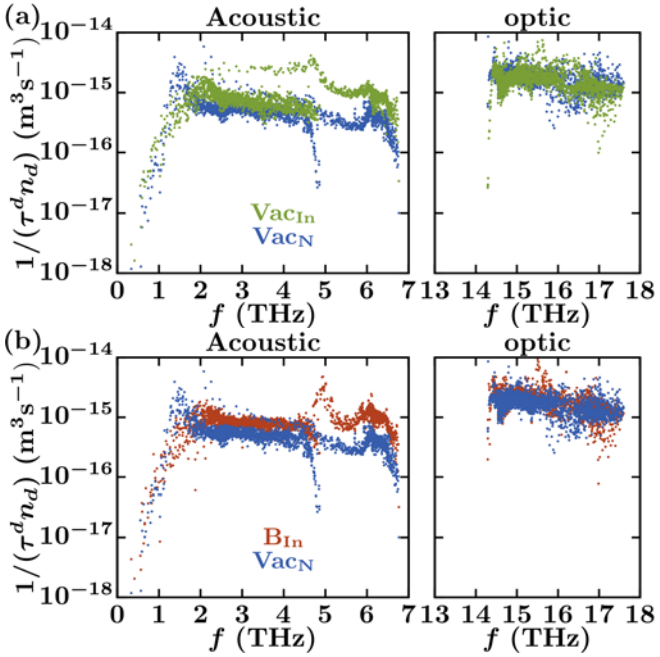

Figure 9: Scattering rates calculated from the Green's function methodology (Eq. 2) scaled by the defect density and including mass and IFC variances. (a) Rates for vacancies used to generate Figure 1. (b) Comparison of the scattering rates due to a B_{In} substitution and a nitrogen vacancy.

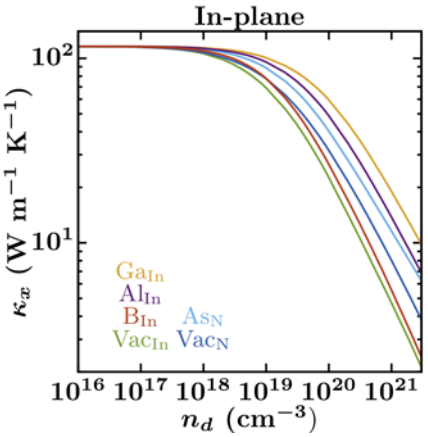

Figure 10: In-plane thermal conductivity of InN with B_{In}, Al_{In}, Ga_{In} or As_N substitutional defects as well as with In or N vacancies.

VI. REFERENCES

[1] G. Srivastava, *The Physics of Phonons* (Taylor & Francis Group, New York, NY, 1990).

[2] S. Tamura, Phys. Rev. B **27**, 858 (1983).

[3] S. Tamura, Phys. Rev. B **30**, 849 (1984).

[4] P. G. Klemens, Proc. Phys. Soc. Sect. A **68**, 1113 (1955).

[5] J. Zou, D. Kotchetkov, A. A. Balandin, D. I. Florescu, and F. H. Pollak, J. Appl. Phys. **92**, 2534 (2002).

[6] M. Asheghi, K. Kurabayashi, R. Kasnavi, and K. E. Goodson, J. Appl. Phys. **91**, 5079 (2002).

[7] H. Malekpour, P. Ramnani, S. Srinivasan, G. Balasubramanian, D. L. Nika, A. Mulchandani, R. K. Lake, and A. A. Balandin, Nanoscale **8**, 14608 (2016).

[8] C. A. Ratsifaritana and P. G. Klemens, Int. J. Thermophys. **8**, 737 (1987).

[9] N. Mingo, K. Esfarjani, D. A. Broido, and D. A. Stewart, Phys. Rev. B **81**, 045408 (2010).

[10] A. Kundu, N. Mingo, D. A. Broido, and D. A. Stewart, Phys. Rev. B **84**, 125426 (2011).

[11] N. A. Katcho, J. Carrete, W. Li, and N. Mingo, Phys. Rev. B **90**, 094117 (2014).

[12] N. H. Protik, J. Carrete, N. A. Katcho, N. Mingo, and D. Broido, Phys. Rev. B **94**, 045207 (2016).

[13] A. Katre, J. Carrete, B. Dongre, G. K. H. Madsen, and N. Mingo, Phys. Rev. Lett. **119**, 075902 (2017).

[14] T. Wang, J. Carrete, A. van Roekeghem, N. Mingo, and G. K. H. Madsen, Phys. Rev. B **95**, 245304 (2017).

[15] C. A. Polanco and L. Lindsay, Phys. Rev. B **97**, 14303 (2018).

[16] A. Katre, J. Carrete, T. Wang, G. K. H. Madsen, and N. Mingo, Phys. Rev. Mater. **2**, 50602 (2018).

[17] R. Stern, T. Wang, J. Carrete, N. Mingo, and G. K. H. Madsen, Phys. Rev. B **97**, 195201 (2018).

[18] K. Y. Kan, C. Yu, D. G. Cahill, and J. Debdeep, Adv. Funct. Mater. **19**, 610 (2009).
[19] A. X. Levander, T. Tong, K. M. Yu, J. Suh, D. Fu, R. Zhang, H. Lu, W. J. Schaff, O. Dubon, W. Walukiewicz, D. G. Cahill, and J. Wu, Appl. Phys. Lett. **98**, 012108 (2011).
[20] J. Wu, J. Appl. Phys. **106**, 11101 (2009).
[21] M. Hase, K. Ishioka, M. Kitajima, K. Ushida, and S. Hishita, Appl. Phys. Lett. **76**, 1258 (2000).
[22] K. Ishioka, M. Hase, M. Kitajima, and K. Ushida, Appl. Phys. Lett. **78**, 3965 (2001).
[23] M. Hase and M. Kitajima, J. Phys. Condens. Matter **22**, 73201 (2010).
[24] P. G. Klemens, Phys. B Condens. Matter **316–317**, 413 (2002).
[25] P. Pobedinskas, B. Ruttens, J. D'Haen, and K. Haenen, Appl. Phys. Lett. **100**, 191906 (2012).
[26] J. M. Ziman, *Electrons and Phonons: The Theory of Transport Phenomena in Solids* (Clarendon Press, Oxford, 2001).
[27] M. Omini and A. Sparavigna, Phys. Rev. B **53**, 9064 (1996).
[28] D. A. Broido, M. Malorny, G. Birner, N. Mingo, and D. A. Stewart, Appl. Phys. Lett. **91**, 231922 (2007).
[29] G. Fugallo, M. Lazzeri, L. Paulatto, and F. Mauri, Phys. Rev. B **88**, 45430 (2013).
[30] L. Lindsay, D. A. Broido, and T. L. Reinecke, Phys. Rev. B **87**, 165201 (2013).
[31] L. Lindsay, Nanoscale Microscale Thermophys. Eng. **20**, 67 (2016).
[32] N. Mingo, D. A. Stewart, D. A. Broido, L. Lindsay, and W. Li, in *Length-Scale Depend. Phonon Interact.*, edited by S. L. Shindé and G. P. Srivastava (Springer New York, New York, NY, 2014), pp. 137--173.
[33] E. N. Economou, *Green's Functions in Quantum Physics*, 3rd ed. (Springer-Verlag Berlin Heidelberg, Berlin, 2006).
[34] N. Mingo and L. Yang, Phys. Rev. B **68**, 245406 (2003).
[35] J.-S. Wang, J. Wang, and J. T. Lü, Eur. Phys. J. B **62**, 381 (2008).
[36] P. Giannozzi, S. Baroni, N. Bonini, M. Calandra, R. Car, C. Cavazzoni, D. Ceresoli, G. L. Chiarotti, M. Cococcioni, I. Dabo, A. D. Corso, S. de Gironcoli, S. Fabris, G. Fratesi, R. Gebauer, U. Gerstmann, C. Gougoussis, A. Kokalj, M. Lazzeri, L. Martin-Samos, N. Marzari, F. Mauri, R. Mazzarello, S. Paolini, A. Pasquarello, L. Paulatto, C. Sbraccia, S. Scandolo, G. Sclauzero, A. P. Seitsonen, A. Smogunov, P. Umari, and R. M. Wentzcovitch, J. Phys. Condens. Matter **21**, 395502 (2009).
[37] T. Feng, L. Lindsay, and X. Ruan, Phys. Rev. B **96**, 161201 (2017).
[38] R. E. Stoller, in *Compr. Nucl. Mater.*, edited by R. J. M. Konings, T. R. Allen, R. E. Stoller, and S. Yamanaka (Elsevier Ltd., Amsterdam, 2012), pp. 293–332.
[39] I. Savic, N. Mingo, and D. A. Stewart, Phys. Rev. Lett. **101**, 165502 (2008).
[40] B. Latour, S. Volz, and Y. Chalopin, Phys. Rev. B **90**, 14307 (2014).
[41] R. Cheaito, C. A. Polanco, S. Addamane, J. Zhang, A. W. Ghosh, G. Balakrishnan, and P. E. Hopkins, Phys. Rev. B **97**, 85306 (2018).
[42] L. Lindsay, W. Li, J. Carrete, N. Mingo, D. A. Broido, and T. L. Reinecke, Phys. Rev. B **89**, 155426 (2014).
[43] L. Lindsay, D. A. Broido, and T. L. Reinecke, Phys. Rev. B **88**, 144306 (2013).
[44] J. Towns, T. Cockerill, M. Dahan, I. Foster, K. Gaither, A. Grimshaw, V. Hazlewood, S. Lathrop, D. Lifka, G. D. Peterson, R. Roskies, J. R. Scott, and N. Wilkins-Diehr, Comput. Sci.

Eng. **16**, 62 (2014).
[45] G. Kresse and D. Joubert, Phys. Rev. B **59**, 1758 (1999).
[46] J. P. Perdew, A. Ruzsinszky, G. I. Csonka, O. A. Vydrov, G. E. Scuseria, L. A. Constantin, X. Zhou, and K. Burke, Phys. Rev. Lett. **100**, 136406 (2008).
[47] J. Serrano, A. Bosak, M. Krisch, F. J. Manjón, A. H. Romero, N. Garro, X. Wang, A. Yoshikawa, and M. Kuball, Phys. Rev. Lett. **106**, 205501 (2011).
[48] K. Esfarjani and H. T. Stokes, Phys. Rev. B **77**, 144112 (2008).
[49] X. Gonze and C. Lee, Phys. Rev. B **55**, 10355 (1997).
[50] V. Y. Davydov, A. A. Klochikhin, A. N. Smirnov, I. Y. Strashkova, A. S. Krylov, H. Lu, W. J. Schaff, H.-M. Lee, Y.-L. Hong, and S. Gwo, Semiconductors **44**, 161 (2010).
[51] V. Y. Davydov, V. V Emtsev, I. N. Goncharuk, A. N. Smirnov, V. D. Petrikov, V. V Mamutin, V. A. Vekshin, S. V Ivanov, M. B. Smirnov, and T. Inushima, Appl. Phys. Lett. **75**, 3297 (1999).
[52] A. Togo, (n.d.).